Deep-Sea Research Part II xxx (xxxx) xxx–xxx

Contents lists available at ScienceDirect

Deep-Sea Research Part II

journal homepage: www.elsevier.com/locate/dsr2

Anatomy of a 'suspended' seafloor in the dense brine waters of the deep hypersaline Urania Basin

I.W. Aiello[a,*], L. Beaufort[b], T. Goldhammer[c,1], V.B. Heuer[c], K.-U. Hinrichs[c], M. Zabel[c]

[a] Moss Landing Marine Laboratories, 8272 Moss Landing Rd., Moss Landing, CA, 95039, USA
[b] Aix Marseille Univ, CNRS, IRD, Coll France, CEREGE, Aix-en-Provence, France
[c] MARUM – Center for Marine Environmental Sciences & Dept. of Geosciences, Univ. of Bremen, D-28334, Bremen, Germany

A B S T R A C T

When micron-sized particles are suspended into the dense brine waters of a deep hypersaline basin, in the absence of biological packaging, their settling velocities should be greatly attenuated. We observed this phenomenon in the anoxic brine water of the Urania Basin in the eastern Mediterranean. We found that the deepest part of this basin is filled with a high-density, about 110 m thick, homogenous fluid mud layer mainly containing microfossils of coccoliths and nannoplankton of Pleistocene and Pliocene age that float in a hot methane-laden brine overlaid by a 'clear' brine. The top of the fluid mud forms a secondary 'suspended seafloor' that has been stable for at least the last two decades since the discovery of the basin. The geochemical characteristics of the fluid mud (e.g. lower salinity than the clear brine, methane-rich) point to a deep source for the fluids, while the age of the microfossils suggests that the floating biogenic particles came from shallower, post-Messinian pelagic deposits such as those exposed along the walls and the rim of the Urania Basin. We hypothesize that catastrophic gravity failures and mass mobilization of the post-Messinian sedimentary layers triggered by earthquake activity are one of the main sources of the sediment in the fluid mud. Because of both, the dense brine fluids, the continuous mixing by thermal convection and the very fine grained nature of the particles, the re-mobilized sediments have never settled, and stay suspended as if they were frozen in time. The prolonged residence time of the supersaturated fluids and the associated microbial activity have also fostered the precipitation of the authigenic gypsum crystals and micron-sized authigenic carbonates that occur mixed with the fluid mud sediments.

1. Introduction

Settling and resuspension of particles are two major antagonistic processes in marine sedimentation. Ultimately, the settling of particles outcompetes resuspension and sediment is deposited on the seafloor. However, deep hypersaline ocean basins could be a special case where settling of very fine particulate matter is attenuated and the antagonists come to a balance. In these unique environments, the long residence time of the particles in suspension allows for prolonged reaction time of biogeochemical processes, and importantly, physical modifications (e.g. carbonate test dissolution, formation of secondary minerals) that imprint the sedimentological regime.

The global distribution of pelagic sediments reflects patterns of primary productivity and settling of biogenic particles and distribution of wind-driven or fluvial siliciclastic particles occurring in the overlying surface waters. Deep-sea sediments mirroring the distribution of particles in the overlying waters is in apparent contrast with settling velocities for finer silt-sized particles, which settle extremely slowly according to Stoke's Law and would be either resuspended by turbulence or dispersed by currents or just dissolved before settling. However, marine particles do settle much faster than the theory would predict (Stokes Paradox), especially after agglomeration into fecal pellets and coagulation (Eppley and Peterson, 1979; Burd and Jackson, 2009). During downward water column transit, this accelerated vertical rain of particles is modified across chemical gradients (e.g., the carbonate compensation depth) and by microbial activity, and further modified by early diagenetic mineralization reactions once the particles reach the seafloor to form water-saturated fluffy deposits known as 'oozes' (Hesse and Schacht, 2011).

While the transit of particles through the water column occurs relatively undisturbed, bioturbation and resuspension can remobilize the sediment after deposition, and sediments advected from the seafloor or subseafloor can become an important source of particles cycled back into the water column. Bottom currents, internal waves, and eddies can increase turbulent mixing in bottom layers and cause lateral advection of particles along isopycnals creating nepheloid layers whose thickness can be up to ~1 km thick (Inthorn et al., 2006; McCave, 2008). Sediment focusing and/or bottom-current induced resedimentation have been observed in open ocean basins worldwide. Resedimentation can produce contourite drift deposits (e.g. Dezileau et al., 2000; Dutkiewicz et al., 2016) or large-scale anomaly in pelagic sediment thickness, which can persist on timescales of millions of years (Dubois and

* Corresponding author.
E-mail address: iaiello@mlml.calstate.edu (I.W. Aiello).
[1] New address: Leibniz Institute for Freshwater Ecology and Inland Fisheries, Department of Chemical Analytics and Biogeochemistry, Berlin, Germany.

https://doi.org/10.1016/j.dsr2.2019.07.014
Received 29 January 2019; Received in revised form 7 July 2019; Accepted 20 July 2019

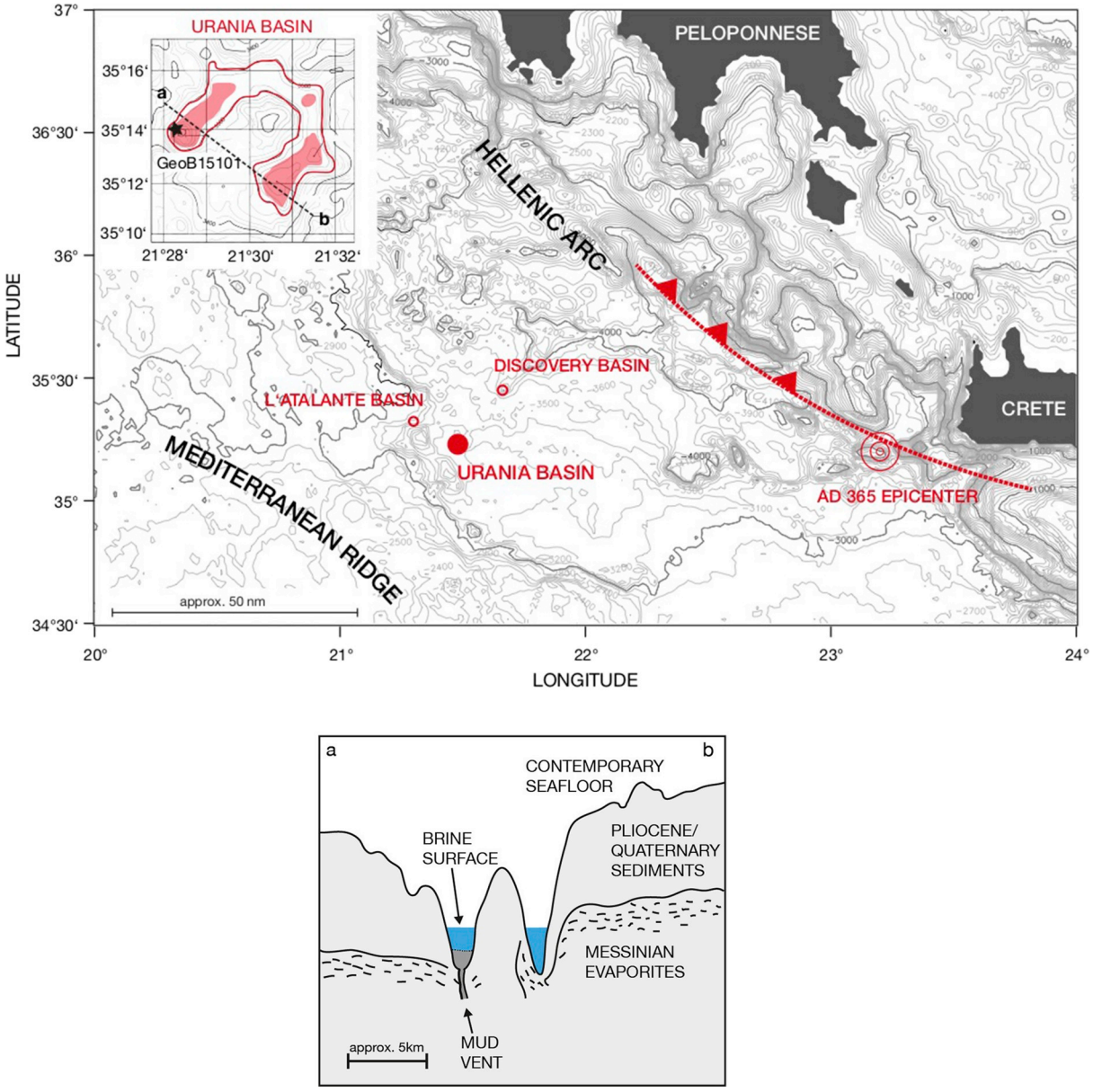

Fig. 1. A) Regional tectonics and location of the Urania Basin and the neighboring L'Atalante and Discovery deep hypersaline anoxic basins in the eastern Mediterranean. The map shows the inferred location of a large earthquake that stroke the offshore region of Crete on AD 365. The inset in the upper left corner shows the bathymetry of the Urania basin (redrawn after Corselli et al., 1998; Aloisi et al., 2006; Goldhammer et al., 2015), with bottom brines in red. Strike line a-b for the geologic sketch in Fig. 1B; B) Idealized geology for strike line a-b across the two legs of Urania basin. Re-drawn after Goldhammer et al. (2015) based on sparker profiles in Corselli et al. (1996) and Fusi et al. (1996). (For interpretation of the references to color in this figure legend, the reader is referred to the Web version of this article.)

Mitchell, 2012). Even more, massive vertical displacement of buried sediments occurs along faults and associated expulsion of mud breccias and fluidized mud volcanism can occur in conjunction with venting of methane and with dissociating gas hydrates (Kopf et al., 1998).

In seafloors that have underlying fossil salt deposits, depressions can be filled with highly saline waters by intrusion of deeply sourced residual brines or dissolution of exposed fossil salts. These deep hypersaline anoxic basins (DHABs) are environments with unique physical and chemical characteristics where settling and resuspension of sediments is controlled by different rules than for the overlying water columns. DHABs of distinct chemical composition are found in the eastern Mediterranean (MEDRIFF Consortium, 1995; Westbrook and Reston, 2002), where they formed by site-specific dissolution of distinct Messinian evaporitic rocks in the shallow subsurface (gypsum, halite, potassium salts and bischofite) that represent different stages of the evaporitic sequence (Jongsma et al., 1983; Wallmann et al., 1997; Cita, 2006). The DHABs show salinities of up to more than 10X seawater and high concentrations of dissolved chemicals such as sulfide or methane produced by hydrothermal reactions and/or microbial activity (Karisiddaiah, 2000; Yakimov et al., 2007). Advection of buried sediments through mud volcanism can occur either on top of seafloor-piercing salt diapirs in subduction zones as well as along structures formed by spreading of sediments gliding over evaporitic layers in passive continental margins (Loncke et al., 2006; Milkov, 2000). Despite the extreme environmental conditions in DHABs, previous microbiological studies have found evidence of active and diverse prokaryotic life including bacteria, archaea and protists within the hypersaline brines and in the haloclines; the availability of organic particles and reduced chemical compounds in the haloclines fosters high microbial biomass and diversity at these interfaces (Eder et al.,

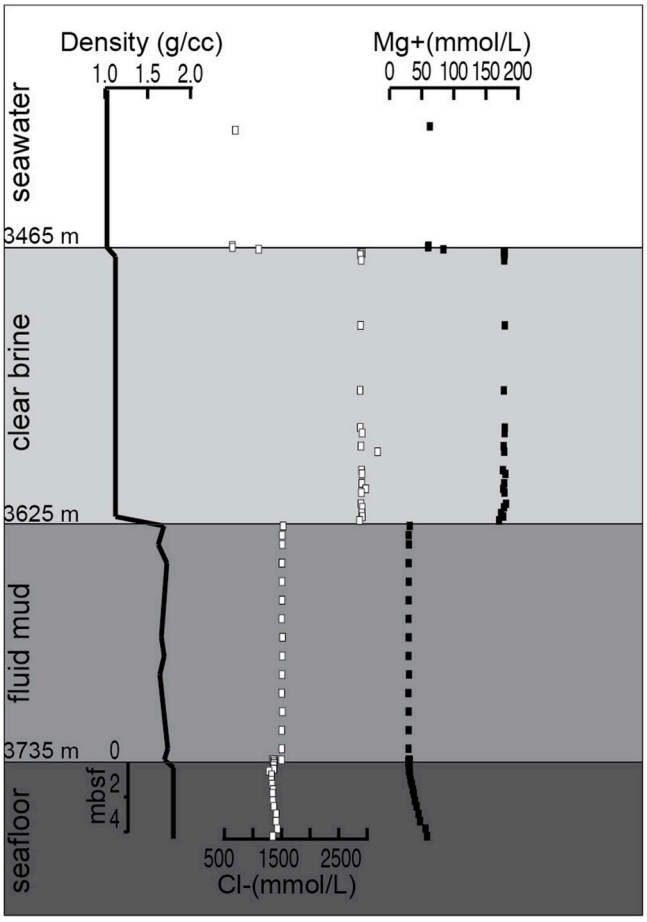

Fig. 2. Density structure and chloride and magnesium composition (Zabel, 2012; Goldhammer et al., 2015) for the Urania Basin (RV Meteor cruise M84/1, Site GeoB 15101). The depths of the top and bottom of the brine (3468 m and 3625 m) are based on CTD's pressure sensor while the depths of the bottom of the fluid mud (3735 m) is based on the length of the cable and approximated to the nearest 5 m.

1999; Van der Wielen et al., 2005; Daffonchio et al., 2006; Borin et al., 2009; Edgcomb et al., 2009). The chemical and physical characteristics of deeply-sourced fluids feeding DHABs, such as the hot, hydrocarbon-rich, muddy brines of the Cheops mud volcano can have significant effects on the diagenetic evolution of the system due to enhanced biogeochemical reactions, including acetate-based methanogenesis, which lead to the precipitation of dolomite and ankerite (Pierre et al., 2014).

2. The Urania Basin

The eastern Mediterranean DHABs are prominently clustered within the Hellenic Subduction Zone in the Mediterranean Ridge, the accretionary prism associated with the Hellenic Arc south of Greece (Fig. 1A). They are thought to have formed by site-specific dissolution of distinct Messinian evaporitic rocks in the shallow subsurface (Jongsma et al., 1983; Corselli and Aghib, 1987; Wallmann et al., 1997; Cita, 2006). Alternatively, Vengosh and Starinsky, 1993Vengosh et al. (1998) proposed a relic origin for the brines of the Urania Basin, from fossil evaporated seawater that was entrapped in Late-Miocene sediments and accumulated in the deep basins of the Mediterranean seafloor.

Among the eastern Mediterranean DHABs, Urania Basin is one of the first discovered and an exemplary site where a direct association between brines and active mud volcanism has been independently documented by exotic deposits sampled in the outer rim of the basin (Hübner et al., 2003), and by the presence of sediments containing Plio-Pleistocene microfossils at the bottom of the basin (Aloisi et al., 2006). The horseshoe-shaped basin is unique due to its depression ('the pit') in the northwestern corner where elevated temperatures of up to 55 °C coincide with active mud volcanism underneath the brine layer (Corselli et al., 1996; Fusi et al., 1996, Fig. 1A and B). With a chloride content of ~2800 mM, i.e., more than five times of that in Mediterranean seawater, Urania Basin brine is the least saline of the Mediterranean DHABs, but contains exceptionally high levels of methane (up to 5.56 mM) and sulfide (up to 16 mM) (Borin et al., 2009), making Urania Basin one of the most sulfidic marine water bodies on Earth (Charlou et al., 2003; Karisiddaiah, 2000; Van der Wielen et al., 2005, Fig. 2).

To explore the consequences of sediment advection through mud volcanism in DHABs, in 2011, RV Meteor cruise M84/1 investigated the geochemical and sedimentological characteristics of the Urania Basin. One of the findings of the expedition was the detection of a layer of suspended mud beneath the clear brine in the western pit of the basin (Fig. 2). The existence of a "very fluid black mud" associated with "a sharp decrease in transmittance and conductivity" was already reported by Corselli et al. (1996) based on CTD data obtained during the original cruise of the R/V Urania that discovered the basin in 1993. The muddy brine layer has a vertical extent (~110 m) that is larger than previously reported (Yakimov et al., 2007; Zabel, 2012). Another notable finding was that the sharp (only 2–3 m thickness) boundaries between seawater, clear brine, and the fluid mud correspond to shifts in temperature and turbidity which depths have remained substantially stable at least since the discovery of the Urania Basin in 1993, and after the Urania Basin was visited again by other scientific cruises (MEDRIFF Consortium, 1995; Corselli et al., 1998; Daffonchio et al., 2006; Borin et al., 2009). The long-term stability of Urania Basin's chemoclines has prompted Goldhammer et al. (2015) to apply a 2-D convection model

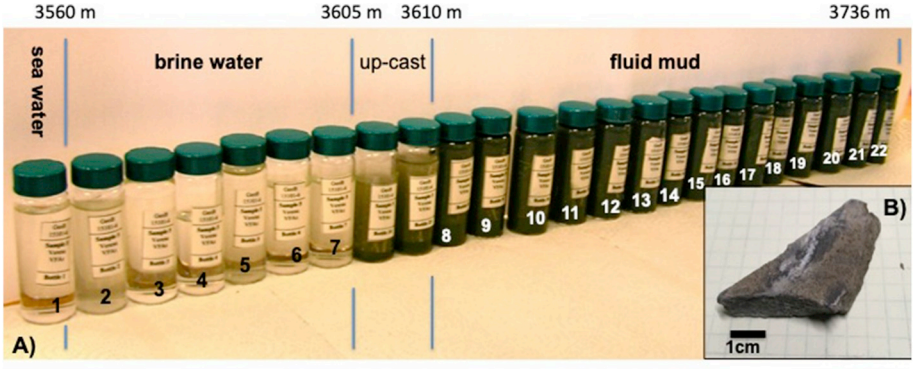

Fig. 3. A) Picture of sample vials taken from the Niskin bottles. The numbers on the bottles correspond to the Niskin cast numbers in Tables 1–4. B) Close-up photograph of an angular and tabular fragment of gypsum retrieved in the bottom part of the gravity core (Sample 15101-7-5 412 cm). Scale bar is next to the sample for reference.

Table 1
Particle size statistics for Niskin bottle and Gravity core samples.

Niskin bottle (cast#6)	Cable depth (m)	Mean (μm)	Median (μm)	Mode (μm)	S.D.	Skewness	Kurtosis	%clay (< 4 μm)	%vf silt (4–8 μm)	%fine silt (8–16 μm)	%medium silt (16–31 μm)	%coarse silt (31–62 μm)	%vf sand (62–125 μm)
8	3610	4.44	5.51	14.94	4.27	−0.62	−0.22	41.38	18.71	20.44	12.03	7.43	0.00
9	3620	4.74	5.88	14.94	4.24	−0.66	−0.15	39.66	18.64	20.62	12.87	8.21	0.00
10	3630	4.82	5.97	14.94	4.31	−0.64	−0.18	39.38	18.35	20.29	13.17	8.80	0.00
11	3640	4.27	5.37	16.40	4.21	−0.68	−0.23	41.98	18.38	20.03	14.87	4.74	0.00
12	3650	4.83	5.92	14.94	4.29	−0.63	−0.17	39.61	18.25	20.28	12.95	8.91	0.00
13	3660	4.68	5.74	14.94	4.22	−0.64	−0.17	40.26	18.55	20.33	12.66	8.19	0.00
14	3670	4.62	5.74	14.94	4.26	−0.65	−0.18	40.31	18.58	20.42	12.80	7.89	0.00
15	3680	4.94	5.95	13.61	4.61	−0.54	−0.31	39.94	17.34	19.20	12.02	10.56	0.94
16	3690	4.73	5.88	14.94	4.28	−0.66	−0.16	39.68	18.53	20.47	12.79	8.53	0.00
17	3700	4.92	5.93	14.94	4.47	−0.57	−0.25	39.80	17.74	19.29	12.47	10.50	0.19
18	3710	4.72	5.80	14.94	4.24	−0.64	−0.16	40.01	18.55	20.34	12.63	8.47	0.00
19	3720	5.03	6.07	14.94	4.41	−0.58	−0.22	39.15	17.90	19.58	12.49	10.71	0.18
20	3730	4.71	5.77	14.94	4.22	−0.64	−0.16	40.09	18.60	20.30	12.66	8.36	0.00
21	3,736	4.25	5.32	16.40	4.18	−0.66	−0.24	42.29	18.35	19.98	14.62	4.76	0.00
mean		4.69	5.77	15.05	4.30	−0.63	−0.20	40.25	18.32	20.11	12.93	8.29	0.09
SD		0.23	0.22	0.65	0.11	0.04	0.04	0.92	0.38	0.43	0.80	1.74	0.24
Gravity core (cast#7)	Depth below seafloor (m)												
	1.80	4.74	5.70	14.94	4.62	−0.52	−0.33	40.90	17.52	18.98	12.26	9.59	0.75
	2.40	4.60	5.51	14.94	4.49	−0.54	−0.30	41.55	17.94	19.05	12.13	9.14	0.19
	3.40	4.34	5.32	14.94	4.25	−0.61	−0.23	42.20	18.76	20.10	12.19	6.74	0.00
	4.02	4.54	5.39	14.94	4.44	−0.53	−0.28	42.01	18.21	18.94	11.82	8.83	0.19
	4.40	4.36	5.22	13.61	4.51	−0.51	−0.34	43.01	17.91	18.91	11.58	8.38	0.21
mean		4.52	5.43	14.67	4.46	−0.54	−0.29	41.93	18.07	19.20	12.00	8.54	0.27
SD		0.17	0.18	0.59	0.13	0.04	0.04	0.78	0.46	0.51	0.28	1.10	0.28
All samples mean		4.61	5.60	14.86	4.38	−0.58	−0.25	41.09	18.19	19.65	12.46	8.41	0.18
All samples SD		0.20	0.20	0.62	0.12	0.04	0.04	0.85	0.42	0.47	0.54	1.42	0.26

Table 2
Results of semiquantitative compositional analyses using smear slide petrography on Niskin bottle and Gravity core samples.

Niskin bottle (cast#6)	Cable depth (m)	Diatoms	Forams	Coccoliths and nanno	Volcanic glass	Clay minerals	Opaques	Celestite	Siliciclastic	Gypsum
8	3610	0.00	0.00	26.80	2.75	1.03	18.90	2.75	20.27	27.49
9	3620	1.19	0.00	26.19	4.76	1.19	19.05	5.95	21.43	20.24
10	3630	0.00	0.81	39.02	2.85	0.00	18.70	3.66	13.82	21.14
11	3640	0.61	0.00	29.09	6.06	1.21	15.76	7.88	18.18	21.21
12	3650	0.00	0.00	28.37	3.55	2.13	19.15	4.96	19.86	21.99
13	3660	0.00	0.00	30.60	5.22	0.75	17.91	5.97	15.67	23.88
14	3670	0.00	0.00	39.34	0.00	0.00	22.95	3.83	11.48	22.40
15	3680	0.00	1.14	32.00	8.57	0.00	18.86	3.43	14.29	21.71
16	3690	0.00	0.00	25.17	4.76	0.00	18.37	5.44	19.05	27.21
17	3700	0.00	0.00	25.47	2.83	0.94	20.75	5.66	16.04	28.30
18	3710	0.00	0.00	28.37	3.55	0.71	17.73	4.96	16.31	28.37
19	3720	0.00	0.00	28.67	6.67	2.67	16.67	4.67	14.67	26.00
20	3730	0.00	0.00	25.00	3.85	0.00	17.31	7.69	22.12	24.04
21	3,736	0.00	0.00	31.98	4.07	0.00	15.70	5.81	23.84	18.60
Gravity core (cast#7)	Depth below seafloor (m)									
	0.6	0.46	0.00	23.74	6.39	10.05	8.68	5.02	18.72	26.94
	1.42	1.17	1.75	17.54	5.85	7.02	13.45	5.26	22.81	25.15
	1.80	2.60	2.60	22.92	1.04	7.81	8.33	5.21	26.56	22.92
	2.8	0.00	0.65	23.87	7.10	0.65	16.13	5.16	18.71	27.74
	2.40	0.00	0.00	26.02	3.25	3.25	14.63	6.50	18.70	27.64
	3.40	0.00	0.00	28.93	5.08	8.63	11.17	5.08	19.29	21.83
	4.40	0.00	0.00	41.92	1.80	0.60	17.96	4.19	16.77	16.77
	5.40	0.00	0.00	26.67	7.18	8.21	10.26	6.15	16.41	24.62
Average Fluid Mud		0.13	0.14	29.72	4.25	0.76	18.41	5.19	17.64	23.76
Average Core Sediment		0.53	0.63	26.45	4.71	5.78	12.58	5.32	19.75	24.20
All samples average		0.33	0.38	28.09	4.48	3.27	15.50	5.26	18.69	23.98

coupled with a 1-D diffusion model to test the hypothesis that these gradients can exist over long periods due to the continual homogenization of the mud and the brine layers by thermal convection. The authors demonstrated that the sharp stratification can be achieved by a coupled diffusion-convection system, and the model runs suggest that the origin of the Urania Basin stratification could be linked to a major earthquake in the region dated to 1650 years B.P. In temporally stable hypersaline marine basins such as Urania, settling and sedimentation of particles can be either greatly decelerated or, for some of the smallest particles, completely stalled by both enhanced viscosity and thermal convection. Unlike under 'normal' seawater conditions characterized by relatively rapid settling, the prolonged residence time in the hypersaline fluid could directly control the available reaction time of fluid-mineral interactions, such as the dissolution of microfossils, and the

Table 3
Results of the filtration experiments carried out to calculate the density of fluid mud samples.

Niskin bottle (cast#6)	Rope depth (m)	Sediment concentration (g/mL)	Sediment weight volume/ cc	H2O mass (vol * density)	Halite mass (vol * density)	Total Density g/cc
8	3610	0.92550	0.34151	0.65849	0.02143	1.60542
9	3620	0.80660	0.29764	0.70236	0.02286	1.53182
10	3630	0.98773	0.36448	0.63552	0.02069	1.64394
14	3670	0.87145	0.32157	0.67843	0.02208	1.57196
15	3680	0.93113	0.34359	0.65641	0.02137	1.60891
16	3690	0.83943	0.30975	0.69025	0.02247	1.55215
20	3730	1.00625	0.37131	0.62869	0.02046	1.65540
21	3,736	0.93323	0.34437	0.65563	0.02134	1.61021
average						1.59748
SD						0.042906

growth of authigenic crystals in supersaturated solutions (Goldhammer et al., 2015).

The suspended mud as well as the bottom (the 'pit') and the rims of the Urania Basin and associated mud volcanism constitute a fascinating and, to some extent, paradoxical model that might not be unique since DHABs are common both in other areas of the Mediterranean Sea, in the Red Sea (Antunes et al., 2011), and in the Gulf of Mexico (Shokes et al., 1977). In this paper we present the interpretation of sedimentologic, mineralogic and micropaloentological analyses of the particles that were collected during expedition M84/1 from the suspended mud and the sediments cored from the Urania Basin's pit.

3. Methods

3.1. Operations and sample collection

The water column, the brine layer and the underlying mud volcano pit of the Urania Basin were sampled during RV Meteor cruise M84/1 at Site GeoB 15101 (35°13.86′N; 21°28.30′E) with a Niskin rosette sampler equipped with a CTD, multicorer and gravity core (Zabel, 2012; Goldhammer et al., 2015, Fig. 1). The onboard echosounder targeted the apparent seafloor of the Urania Basin at a depth of approximately 3600 m (Fig. 2). A prominent halocline was detected at about 3465 m, and corresponded to a salinity increase from ~39 to ~152 PSU, a 2.5 °C increase in temperature (14–16.5 °C) and the complete depletion of free oxygen (Zabel, 2012). Once the CTD (cast M84/1-GeoB15101-6) reached the depth of the echosounder seafloor, there was no drop of the cable tension so the deployment was continued below that depth (Fig. 2). About 160 m within the brine, at 3625 m rope length, a second density boundary was detected below which the CTD malfunctioned. The length of the rope and the depth indicated by the pressure gauge attached to the CTD rosette diverged below the depth of the second density boundary suggesting the transition to a fluid much denser than seawater or brine fluids (all measurements used in this paper are in rope length). The deployment continued until 3735 m depth, at which we encountered a third boundary that was indicated by a relatively fast decrease of the cable tension. Here, the CTD rosette reached sufficiently consolidated sediments that stopped further sinking. The corresponding water depth of 3735 m was 110 m below the expected seafloor depth based on echosounder data (Zabel, 2012). The samples recovered in Niskin bottles returned clear brine fluids from the 3465 m–3625 m depth interval, but the samples below that interval, over 110 vertical meters, returned a fluid mud (Fig. 3A).

The successive deployment of a gravity corer (cast M84/1-GeoB15101-7) for a total of 9 m which, like the CTD rosette, reached a resistant layer at about 3735 m depth, returned homogenous and soupy sediments in the upper ~5 m and homogenous and firmer sediments below. No sedimentary structures or other noticeable feature were present in the core besides the presence of a large, indurated fragment.

3.2. Particle sizes

The distributions of particle sizes of the samples from both the Niskin rosette and the cores were analyzed using a Laser Particle Sizer Analyzer (LPSA). We used a Beckman-Coulter LS 13 320 (the instrument uses a 5 mW laser diode with a wavelength of 750 nm). This instrument analyzes small (~0.5–2.0 g) masses of unconsolidated sediment and combines conventional laser beam diffraction with polarized intensity differential scattering allowing highly resolved grain size measurements (126 logarithmically spaced channels between 0.04 μm and 2.00 mm; Beckman Coulter Inc., 2003). Laser diffraction particle-size measurement is based on the Fraunhofer and Mie theory of light scattering, whereby spherical particles of a given size diffract light at a specific angle, with the angle increasing with decreasing particle size (Singer et al., 1988). Geometric statistics were applied to the values obtained by the logarithmically spaced size channels of the particle analyzer using the method of moments, since the samples tend to have log-normal grain size distributions in the 0.04 μm to 2 mm spectrum. Samples were run at least in triplicate and the results were averaged. This analytical method has successfully been used on core sediments of mixed biogenic and siliciclastic composition (Aiello and Ravelo, 2012) and siliciclastic sediments (Fildani et al., 2018). The sample is diluted in a 1.2 L aqueous module filled with deionized water equipped with a pump unit running at 100% power. The sample is added to the module until optimal obscuration conditions are reached. Previous experiments have suggested that in samples mixed with clay and silt, standard obscuration conditions might not capture the full extent of the particle size distribution (Fildani et al., 2018). With increasing obscuration conditions a larger range of particles is measured until an optimal concentration is reached. Preliminary tests indicated that disaggregation of the sample (e.g. using sonication) prior to the analysis was unnecessary and that the energy of the water controlled by the pump was sufficient to ensure complete disaggregation and that the optimal obscuration value was between 10 and 15%. A disadvantage is the limit of the maximum measurable grain size (2000 μm), and previous studies have shown that the analysis of the distribution of the fine-grained fraction (clay and fine silt) is less accurate in LPSA compared to settling methods (e.g. Konert and Vandenberghe, 1997). The platy shape of clay affects the light scattering such that the instrument returns a larger size, potentially resulting in an underestimation of the clay fraction. However, McCave et al. (2006) demonstrated that differences in estimates of the mean and relative percentage of the silt and finer grain-size fraction from LPSA versus settling methods were negligible. The statistical results of the LPSA are summarized in Table 1.

3.3. Particle composition

A total of 22 samples from the Urania fluid mud and from the pit (the consolidated, underlying sediments at the same location) were analyzed using smear slide petrography with a transmitted-light petrographic microscope equipped with a standard eyepiece micrometer (Table 2). Biogenic and mineral components were identified based on their shapes and optical properties and their percentage abundances were visually estimated (methods in Rothwell, 1989). To improve the reproducibility of the analysis, 10 counts were done on different parts of a smear slide using a random walk and the average value of the 10 counts was used. Fields of view having too little (< 10% coverage) or too much (> 30% coverage) material were not measured.

To further investigate the types and compositions of the sediment samples collected in the Urania Basin a subset of samples was analyzed using Scanning Electron Microscopy (Hitachi S-3400N-II variable pressure SEM) equipped with an INCA Energy 250 energy dispersive X-ray spectrometer (EDX). SEM samples were prepared by placing < 1 g of wet sediment on a pedestal and drying in a fume hood, a copper

Table 4
Calcareous nannofossil species occurrence in the studied samples. One cross indicates the presence of a taxa, and two crosses indicate the relative high abundance (> 30%) of the taxa in the nannofossil assemblage.

Bottles CTD cast#6	Rope depth (m)	Coccolithophores												
		E.huxley	*G.ericsonii*	*G.muellerae*	*G. oceanica*	*G.caribbeanica*	*H. carteri*	*P. multipora*	*S. pulchra*	*Oolithotus*	*C. leptoporus*	*Hyaster perplexus*	*Calciosolenaia*	*Ceratolithus cristatus*
8	3610	x	xx	x	x	x	x	x	x					
9	3620	x	xx	x	x	x	x				x			
10	3630	xx	x	x	x	x	x							
11	3640	x	x		x		x				x			
12	3650	x	x		x			x						
13	3660	x	x	x	x	x	x		x		x			x
14	3670	x	x	x	x	x	x		x			x		
15	3680	x	x	.	x	x	x				x	x		
16	3690	x	x	x	x	x	x				x			
17	3700	x	x		x	x	x				x		x	
18	3710	x	x		x		x			x				
19	3720	x	x		x									
20	3730	x	x	x	x	x	x	x	x			x		
21	3,736		x		x	x	x	x			x			
Gravity core (cast#7)	Depth below seafloor (m)													
	0.6	x	x	x	x	x	x		x		x			
	1.42		x	x	x	x	x				x			
	1.80		x	x	x	x	x							
	2.8		x	x	x	x	x							
	2.40		x	x	x	x	x							
	3.40		x	x	x	x	x							
	4.40		x	x	x	x	x							
	5.40		x	x	x	x	x							

Bottles CTD cast#6	Coccolithophores	Pliocene nannofossils												
	R.clavigera	*D. pentaradiatus*	*D.variabilis*	*D. tamalis*	*D.asymetricus*	*D.surculus*	*D. brouweri*	*D.triradiatus*	*C. pelagicus*	*H.sellii*	*Calcidiscus macintyrei*	*Pseudoemil lacunosa*	*Reticulofenestra pseudoumbilica*	*Sphenolithus abies*
8		x	x			x			x	x	x	x		
9		x		x		x			x	x	x			
10	x	x				x			x		x		x	
11	x	x	x		x	x	x		x	x		x	x	
12		x		x	x	x		x	x					
13		x				x				x	x	x	x	
14		x	x			x			x	x	x	x	x	
15		x		xx		x			x		x	x	x	
16		x	x	x	x	x			x	x	x	x	x	x
17	x	x	x	x						x	x		x	
18						x			x	x	x	x	x	
19		x		x		x	x					x	x	
20											x	x	x	
21	x		x			x			x	x			x	x

(*continued on next page*)

Table 4 (*continued*)

Bottles CTD cast#6	Coccolithophores				Pliocene nannofossils										
	R.clavigera	*D. pentaradiatus*	*D.variabilis*	*D. tamalis*	*D.asymetricus*	*D.surculus*	*D. brouweri*	*D.triradiatus*	*C. pelagicus*	*H.selliti*	*Calcidiscus macintyrei*	*Pseudoemil lacunosa*	*Reticulofenestra pseudoumblica*	*Sphenolithus abies*
Gravity core (cast#7)														
		+	+	+	+	+	+	+	x					
		+	+	+	+	+	+	+						
		+	+	+	+	+	+	+	x	x	x			
		+	+	+	+	+	+	+	x		x		x	
		+	+	+	+	+	+	+			x			
		+	+	+	+	+	+	+	x		x		x	
		+	+	+	+	+	+	+			x			
		+	+	+	+	+	+	+	x		x		x	
		+	+	+	+	+	+	+			x			

Note: the number of 'x' represent the relative abundance for of each taxa.

standard was attached to each sample for EDX calibration. The EDX was used to produce semi-quantitative estimates of the elemental composition of single features as well as to map out elements over the entire field of view (see 'Results' section).

The samples were also analyzed for mineralogic composition using a Rigaku SmartLab SE X-Ray Diffractometer (XRD) equipped with a D/teX Ultra 250 0D/1D compound silicon strip high speed detector and the ICDD PDF-4 + Database phase identification software. XRD sample preparation was carried out using standard laboratory procedure (Poppe et al., 2001). The dried samples were ground twice for 10 min at a time and sieved through a 63 μm mesh to ensure that all grains were of uniform small dimensions. Bulk mineralogy of the samples was determined with a randomly oriented powder mount technique (Poppe et al., 2001). Operating conditions included: Cu Kα Ni filtered radiation, 40 kV accelerating voltage and 30 mA current. All samples were analyzed over the angular range $3 \leq 2\boldsymbol{\theta} \leq 85$, with a step increments of 0.001 $2\boldsymbol{\theta}$, and a counting time of $1\boldsymbol{\theta}$ per minute.

3.4. Density of the fluid mud

The density of the fluid mud sampled with the Niskin bottles was calculated for 8 of the bottles by measuring the concentration (g/ml) of the suspended particulate through filtration. Aliquots (between 200 and 350 μl) of the Niskin samples were vacuum filtered using pre-weighted MF-Millipore Membrane hydrophilic filters with 0.45 μm pore size, and each sample was filtered and weighted in triplicate (Table 3). Using a salinity value for the seawater in the fluid mud similar to that of the clear brine (160 ppm) and the specific density of halite (2.6 g/cc), the total density of the sample was calculated by adding the concentration of suspended sediment to the density of the salt (Table 3).

3.5. Microfossils

Water samples were let settle in petri dishes containing a coverslip at their bottom for 4 h. After the water was removed, the dry coverslips were mounted on microscopic slides, and observed on a Leica Polarizing Microscope with a x100 lens. Eight sediment samples from cast M84/1-GeoB15101-7 were smeared onto slides and mounted with coverslips. Two sets of slides were prepared: one with little amount of sediment to get a low particle density that permitted observation of separated particles. The other set was prepared with larger amount of sediments in order to detect rarer large nannofossils such as Discoaster specimens. Results are shown in Table 4.

3.6. Geochemistry

Water and fluid samples from Niskin bottle hydrocasts were filtered by rhizon samplers (0.1 μm filter width) and refrigerated for onshore analysis. Dissolved inorganic carbon was measured by infrared spectroscopy after liberation of CO_2 by acid purge (Analytik Jena multiN/C 2100). Dissolved chloride and sulfate were determined by ion chromatography (Metrohm CompactIC) in samples diluted 1:100 with Milli-Q grade water. Dissolved total elemental contents of boron (B), calcium (Ca), potassium (K), magnesium (Mg), sodium (Na), sulfur (S), and silicium (Si) were determined by inductively coupled plasma-optical emission spectrometry in samples diluted 1:10 or 1:100 with 1% ultrapure HNO_3. Table 5 summarizes the hydrocast data at site GeoB15101 of major chemical parameters including: dissolved inorganic carbon (DIC), dissolved chloride, dissolved sulfate, and total dissolved elemental contents of boron (B), calcium (Ca), potassium (K), magnesium (Mg), sodium (Na), sulfur (S), and silica (Si). Concentrations are in millimoles per liter. The postulated seawater-brine interface is located between 3461 and 3463 m water depth, the postulated brine/fluid mud interface between 3607 and 3610 m water depth.

Table 5
Summary of the hydrocast data for major chemical parameters measured at site GeoB15101.

water depth	DIC	Chloride	Sulfate	B	Ca	K	Mg	Na	S	Si
m	*mM*	*mM*	*mM*	*mM*	*mM*	*mM*	*mM*	*mM*	*mM*	*mM*
70	2,5	612		0,45	11,8	11,1	61,3	526	32,1	0,002
320	2,6	620	35,6	0,46	11,9	11,3	62,1	534	32,7	0,002
566	2,5	613	35,3	0,45	11,8	11,2	61,6	529	32,3	0,004
1000	2,7	614	37,6	0,46	11,8	11,1	61,5	528	32,0	0,010
2001	2,6	613	36,5	0,46	11,8	11,1	61,2	526	32,2	0,009
3000	2,7	873		0,50	11,9	10,6	64,1	529	40,7	0,015
3459	2,7	610	35,4	0,46	11,9	11,3	61,9	531	32,1	0,010
3460	2,9	614	36,7	0,49	11,8	11,4	61,5	533	32,3	0,012
3461	8,2	1063	48,1	2,09	17,9	25,4	84,6	933	47,0	0,208
3463	32,9	2829	95,6	8,57	42,4	78,8	176,7	2454	95,4	0,956
3464	32,7	2819	94,9	8,57	42,6	79,6	177,2	2464	95,1	0,955
3467	33,1	2821	96,4	8,51	42,5	79,0	176,9	2458	95,8	0,965
3502	33,4	2809	93,8	8,58	42,8	79,3	177,8	2474	96,1	0,969
3537	32,1	2801	95,5	8,50	42,4	79,0	176,3	2456	95,8	0,967
3557	32,9	2802	94,7	8,60	42,7	79,5	177,8	2474	96,2	0,959
3560	30,1	2836		8,48	42,6	79,6	177,4	2459	97,4	0,955
3567	33,8	2815	96,2	8,52	42,4	78,1	175,9	2447	95,0	0,952
3570	30,2	3102		8,54	42,4	78,8	176,8	2449	95,6	0,966
3580	29,4	2825		8,41	42,0	78,2	174,8	2422	95,3	0,942
3582	33,3	2834	95,0	8,61	42,8	79,6	178,7	2477	95,8	0,972
3587	31,3	2829	93,8	8,54	37,6	78,3	176,8	2468	96,5	0,955
3590	30,1	2896		8,45	42,1	77,9	175,5	2437	95,1	0,949
3592	33,2	2822	94,1	8,53	41,4	79,1	177,1	2467	95,9	0,973
3598	33,0	2815	95,8	8,72	43,0	80,6	179,6	2493	96,7	0,998
3600	29,7	2837		8,51	42,4	78,1	176,6	2442	96	0,956
3603	27,8	2829		8,45	42,1	76,4	172,2	2393	95,1	0,949
3605	29,3	2840		8,48	41,8	78,1	175,3	2422	96,5	0,942
3607	28,7	2791		8,46	42,7	74,8	169,1	2373	93,6	0,957
3610		1482		7,95	50,1	24,2	33,5	1253	55,2	1,283
3615	17,7	1465		8,00	49,4	22,2	31,9	1219	52,4	1,301
3620	14,5	1466		8,01	49,1	22,2	32,3	1232	53,3	1,293
3630		1462		7,92	48,7	22,3	31,9	1229	52	1,28
3640		1463		8,04	49,4	22,4	32,1	1235	53,3	1,283
3650		1463		7,98	49,4	22,3	32,0	1227	53,1	1,293
3660	18,0	1456		7,99	49,2	22,1	31,8	1216	52,7	1,303
3670		1472		8,01	49,3	22,3	31,9	1222	52,9	1,292
3680	18,2	1467		7,97	49,1	21,9	31,8	1218	52	1,294
3690		1463		7,88	49,0	21,8	32,4	1214	52,5	1,275
3700	18,2	1459		7,95	49,4	22,1	31,7	1214	52,6	1,303
3710	17,6	1469		7,97	49,3	22,2	31,9	1216	53,1	1,299
3720	19,6	1459		8,04	49,9	22,2	32,0	1218	52,6	1,316
3730		1459		7,97	49,0	22,1	31,8	1216	52,8	1,282
3736	17,7	1454		7,85	49,1	21,6	32,3	1202	52,6	1,288

4. Results

4.1. Particle texture, composition and physical properties

The most striking result of the sedimentologic analysis of the particles in the fluid mud and the core sediments is that the grain size distribution in the fluid mud does not differ from the sediment in the core. All samples analyzed have a mean size of 4.61 ± 0.20 μm, are negatively skewed, their standard deviation is 4.80 ± 0.12 μm, and the median is 5.60 ± 0.20 μm (Table 1). All frequency plots, whether they are for the Niskin bottles samples (Fig. 4A) or the core samples (Fig. 4B), are characterized by a tri-modal distribution: the main mode is centered at ~15 μm, the secondary mode is ~5 μm (close to the mean value) and the smallest mode is ~40 μm. The main mode corresponds to the grain size boundary between very fine silt and medium silt, and the area under the half-width of the modal peak (~15 ± 5 μm) includes ~20% of the grain size population. The majority of the particles (~60%) is silt size (4 < and ≤63 μm), ~40% is clay size (≤4 μm), and sand size particles (> 63 μm) occur only in trace amounts.

Smear slide microscopy together with SEM-EDX microscopy and XRD were used to identify the modal fractions (Figs. 5–7). As observed for the grain size distributions, the compositions are similar to all samples whether they are from the fluid mud or from the core. The most common group of particles is represented by biogenic carbonates, either coccoliths or nannoplankton (~30%; Table 2; Figs. 5 and 6). However, not all carbonate particles are biogenic, including micron-sized rhombohedric, subspherical or elongated dolomite particles (Fig. 6A and B). These particles resemble micron-sized authigenic carbonates observed in other environments where mud volcanism is present (e.g. the Nile deep sea fan; Pierre et al., 2014) and similarly, they are probably the byproducts of microbial activity. The other two common particle types are gypsum (~23%; Figs. 5 and 6; Table 2) and siliciclastics (primarily quartz, feldspars and micas; ~18%; Fig. 5A and B; Fig. 6; Fig. 7A, and B), which are mainly silt-sized, although sand-size siliciclastic particles have also been observed. Volcanic shards (~5%) and rare foraminifer tests (< 1%) are other minor component of the silt-sized particles (Fig. 5A, and B; Fig. 6E and F). Opaques particles that result completely opaque both under plain- and cross-polarized light include sulfides and iron oxides and they occur mainly in the very fine silt and clay fractions (~15%). Other minerals observed but that occur only in trace amounts include celestite ($SrSO_4$; Fig. 7A, and B), clay minerals and fragments of diatoms and silicoflagellates.

The XRD analyses of the bulk sediments for 4 samples from the gravity core and 2 samples from the Niskin bottles (Table 2) are in general agreement with the compositional analyses done with smear slide petrography and SEM-EDX, with the most common minerals being

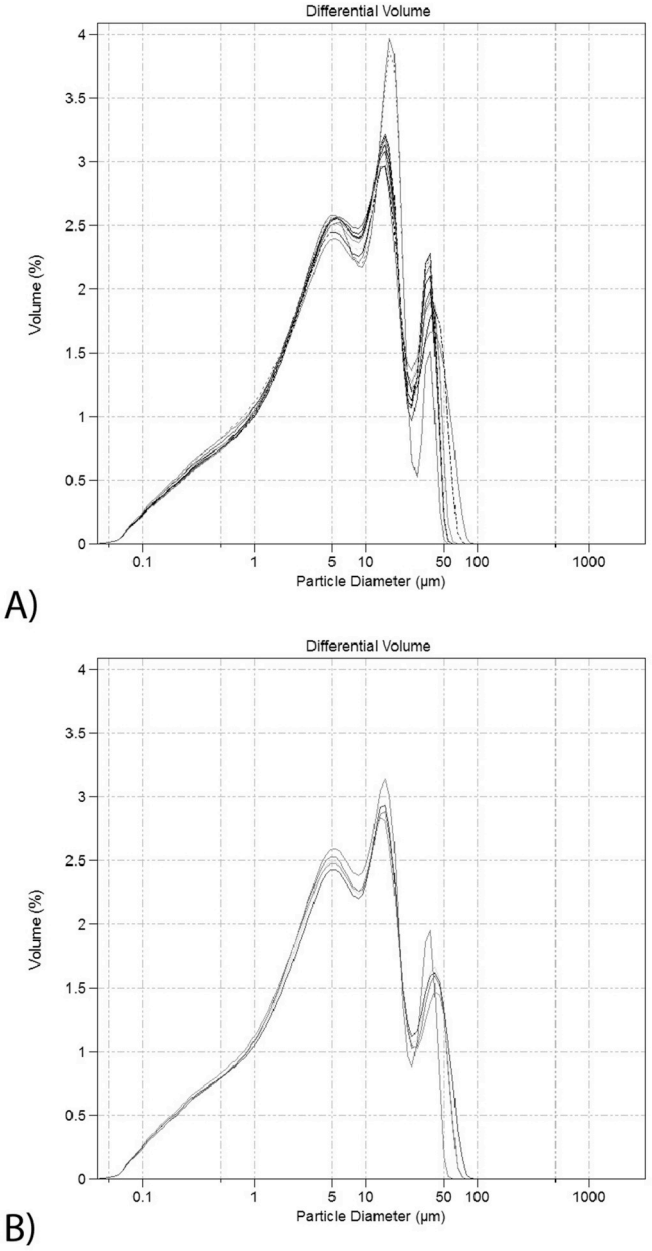

Fig. 4. Frequency plots representative of all Urania Basin samples analyzed. A) Samples from the fluid mud; B) Core samples.

dolomite (25–35%), quartz (21–36%), calcite (14–19%) and gypsum (15%). Halite, muscovite, albite, chlorite, elemental sulfur, sulfides and clay minerals were also identified but were quantified only in trace amounts (< 5%).

Most gypsum particles are silt-size, subrounded, and tabular (Fig. 5). Less commonly, the crystals of gypsum are euhedral, and coarse silt or very fine sand in size. A tabular, ~5 × 1 cm indurated, angular fragment mainly composed of anhydride (~68%) and secondarily gypsum (~28%) and trace amounts of quartz, clay minerals and biosilica was found in the bottom part of the gravity core (Sample 15101-7-5 412 cm; Fig. 3B; Fig. 7C–F). The SEM-EDX analysis of the fragment shows that the anhydride/gypsum crystals precipitated within a fine-grained Si-rich matrix mainly composed of whole or fragmented diatom tests (Fig. 7E and F). The composition of the matrix is dramatically different from the composition of the particles in the fluid mud and the sediment recovered by coring, but it is similar to biosilica-rich deposits observed in the region including the nearby Discovery Basin (Zabel, 2012) and to the crystalline and/or laminated diatom-gypsum deposits recovered at the DSDP Site 374 in the Ionian Basin (Hsü et al., 1978).

The fluid mud has a much higher density than the brine (~1.6 g/cm^3 ± 0.04 compared to 1.13 g/cm^3 in the brine). The density of the fluid is comparable, for instance, with the bulk-saturated density of pelagic sediments having similar composition (Fusi et al., 1996). The density of the samples collected with the Niskin bottle does not change over the 110 vertical meters of the fluid mud (Table 3; Fig. 2). The water content in the fluid mud ranges between ~61% and 69% (Table 2) which is above the Atterberg's liquid limit measured for similar sediments recovered during Leg 160 at the Olimpi Mud Volcano field (Kopf et al., 1998).

4.2. Nannofossils

The calcite placoliths show various degrees of preservation and are derived from a mix of Pliocene nannofossils and Pleistocene coccolithophorids. The Pliocene specimens are commonly very recrystallized. The taxa found in the fluid mud are similar to those found in a core collected in Urania Basin by Aloisi et al. (2006), with the main difference that no specimens of the genus *Amaurolithus* (late Miocene, early Pliocene) were observed (Fig. 8; Table 4). The nannofossils are a mixture of two assemblages. A first assemblage (see bottles 8 to 10; Table 4) is dominated by *Gephyrocapsa ericsonii* (Fig. 8B) and includes commonly large (> ~4 μm) placoliths of *Emiliania huxleyi* (Fig. 8A). Fragile specimens of *Syracosphaera pulchra*, *Oolithotus*, and *Hyaster perplexus* are also commonly observed. The assemblage can be dated to the Marine Isotope Stages (MIS) 7 to 5 and possibly MIS 6 because of the large *E. huxleyi,* which are usually found in glacials (Triantaphyllou et al., 2009), and the abundance *G. ericsonii* that peaks between MIS7 and MIS5 (Pujos and Giraudeau, 1993). The second assemblage (e.g. bottle 15; Table 4) can be dated broadly between 3.7 and 3.8 Ma based on the presence of *Discoaster tamalis* (appearing at 3.85 Ma) and *Reticulofenestra pseudoumbilicus* (disappearing at 3.7 Ma) and of other coccoliths of the extinct genus *Discoaster* (Fig. 8C and D). The relative abundance of *Discoaster* specimens in the bottom 4 bottles (bottle 18 to 21) is lower probably due to a lack of preservation. No Miocene taxa belonging to the genus *Discoaster* were observed. In general, the taxa found in the gravity core are similar to those found in the fluid mud (Table 4) and, as observed in the bottom 4 bottles of the fluid mud, the abundance of *Discoaster* specimens is much lower that in the water. Specimens of several *Discoaster* species (e.g. *D. tamalis*, *D. assymetricus*, and *D. triradiatus*) were detected only in high density smear slides. The relative proportion of Pliocene and Pleistocene assemblages is different than the one found in the bottles and described by Aloisi et al. (2006).

5. Discussion

5.1. A stable, vertically expanded seafloor

The sedimentologic and mineralogic characteristics and the nannofossil content of the sediment samples recovered in the Urania Basin are similar across the entire thickness (~110 m) of the fluid mud layer and are indistinguishable from the samples from the more consolidated oozes recovered at the bottom of the basin by coring. The geochemical analyses of major dissolved components returned consistently homogenous, sharply differentiated layers of brine and fluid mud in the investigated NW Urania Basin (Fig. 1A; Fig. 2; Table 5). In seafloors worldwide, the transition between the water column and the underlying consolidated sediments is characterized by 'fluffy' ooze layers a few cm thick at most. In the Urania Basin this transition is greatly vertically expanded and together with the geochemical zonation does not occur on a scale of centimeters but of tens of meters.

The existence of the brine layer and fluid mud layer are documented in earlier research in the northwest Urania Basin (e.g., Corselli et al.,

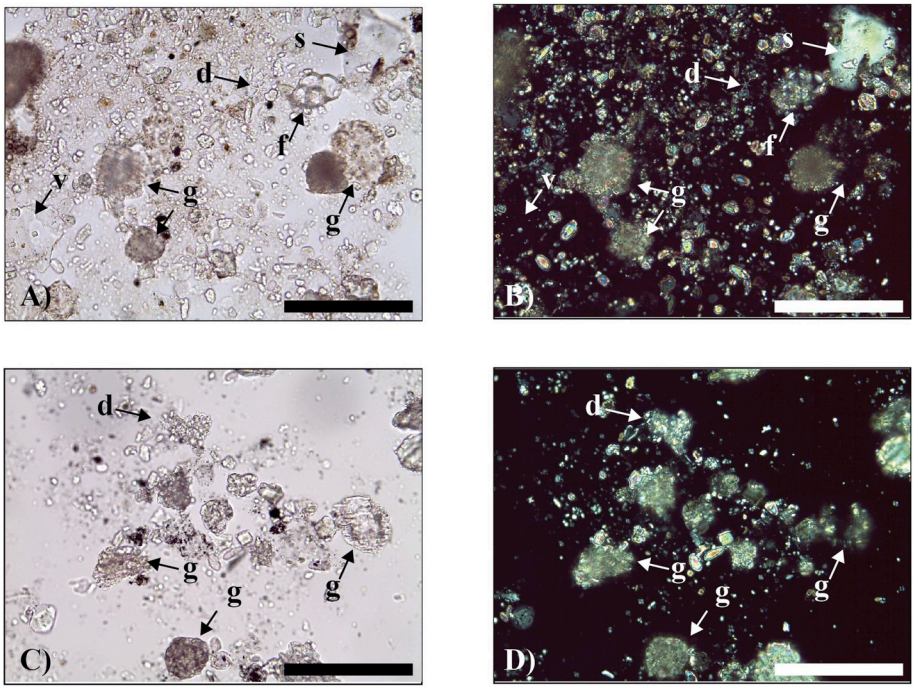

Fig. 5. Microphotographs of petrographic smear slides. Scale bar is 100 µm. A) Plain-polarized and B) cross-polarized view of a sample from the gravity core, 4.4 m below the seafloor (see Table 1 for grain size data). B) and C) are the plane-polarized and cross-polarized microphotographs of a fluid mud sample (Niskin bottle 16; Table 1). The majority of the micron-sized particles in the background are either coccoliths or nannoplankton. Labels used in the figure: g = gypsum, s = siliciclastic particle, d = *Discoaster*, v = volcanic shard, f = foraminifer test.

1998; Hübner et al., 2003; Aloisi et al., 2006; Yakimov et al., 2007). However, these features have not been reported by the earlier work of Vengosh et al. (1998), who investigated the southeast branch of Urania Basin instead. Thermal gradients were not as pronounced, and the brine chemistry was not entirely homogenous through the water column (Vengosh et al., 1998). These differences suggest that the brine layers at the bottom of the NW and SE portion of the Urania Basin horseshoe may be not as connected as previously thought (Corselli et al., 1996).

The other remarkable feature of this system is that depth, salinity, temperature and density gradients of the seawater/brine halocline in the northwest branch of the Urania Basin have not significantly changed since its initial discovery in 1993. For instance, a large temperature increase up to 55 °C together with an 80% drop in light attenuation at the same depth as the top of the fluid mud measured in the Urania Basin in 1994 and 1997 suggest that the fluid mud has been a persistent feature at least for two decades (MEDRIFF Consortium, 1995; Corselli et al., 1996; Corselli et al., 1998; Cita, 2006). The persistence of this boundary over time and the lack of mixing are also supported by the non-gradual and rather sharp change in concentrations of conservative ions such as Mg^{2+} and Cl^{-} (Fig. 2; Table 5; Goldhammer et al., 2015).

5.2. The source of the fluid mud particles

The abundance of Pliocene and Pleistocene nannofossils (Table 4) indicates that the majority of the particles in the fluid mud derive from old marine deposits. However, the particles are not just a simple mixture of nannofossils from these two periods. The dominant sources are sediments from the middle late Pleistocene and the early Pliocene: The first assemblage can be dated to the Marine Isotope Stages (MIS) 7 to 5 and possibly MIS 6 because of the large *E. huxleyi,* which are usually found in glacials (Triantaphyllou et al., 2009), and the abundance of *G. ericsonii* that peaks between MIS7 and MIS5. In the second assemblage (e.g. bottle 15; Table 4), *D. brouweri* and *D. triradiatus*, which are common taxa of the late Pliocene, are rare, while early Pliocene taxa are more abundant (e.g. *D. tamalis, D. asymetricus and D. surculus*). The assemblage can be dated broadly between 3.7 and 3.8 Ma based on the presence of *Discoaster tamalis* (appearing at 3.85 Ma) and *Reticulofenestra pseudoumbilicus* (disappearing at 3.7 Ma) and of other coccoliths of the extinct genus *Discoaster* (Fig. 8C and D). The occurrence of very few instances of *G. caribbeanica* (which is extremely abundant between 0.3 and 0.7 Ma; Toledo et al., 2016) indicates the absence of middle Pleistocene sediments. No Miocene or older taxa were observed.

The lower salinities and Mg-concentrations of the fluid mud compared to the overlying clear brine are in line with a Cl^{-}- and Mg^{2+}-depleted source for the fluids (for instance, fresh subsurface fluids in an accretionary prism; Le Pichon et al., 1991) and consistent with the previous hypothesis suggesting that mud volcanism in Urania Basin was fed by advective transport from a deep fluid reservoir below the Messinian evaporite sequence (Winckler et al., 1997) of warm, methane-rich fluids (Corselli et al., 1996; Fusi et al., 1996; Charlou et al., 2003; Aloisi et al., 2006).

While the geochemistry points to a deep source for the fluids (Winckler et al., 1997), the composition of the particles in the fluid mud and in the cores is not conclusive as to what their source(s) are. The silt size particles of gypsum (the second most abundant component in both fluid mud and core sediments) are for the majority non-euhedral indicating that they either have formed in place, they have been transported or they have partially been dissolved as a consequence of Anaerobic Oxidation of Methane (AOM). The occurrence of active microbial processes such as the AOM is supported by the presence of micron-sized dolomite precipitates similar to precipitates observed in other DHABs (e.g. Pierre et al., 2014). In turn, the occurrence of the dolomite precipitates supports the suggestion of Goldhammer et al. (2015) that the long residence time of the fluid mud can promote authigenesis directly in the water column. The euhedral crystals of celestite in the fluid mud could have been transported from the subseafloor where they were formed as a result of diagenesis of pelagic carbonate sediments although they have also been found associated with gypsum and other evaporitic minerals so they could have been formed *in situ* (Baker and Bloomer, 1988).

The lack of Miocene or older nannofossils in the fluid mud is, to a certain extent, surprising: if fluids and particles were originated from the same deep reservoir, the fluids would have entrained biogenic particles of Messinian age or older. Conversely, the coccoliths and nannofossil taxa present in the fluid mud are more compatible with younger and shallower sedimentary deposits, such as the Pliocene and

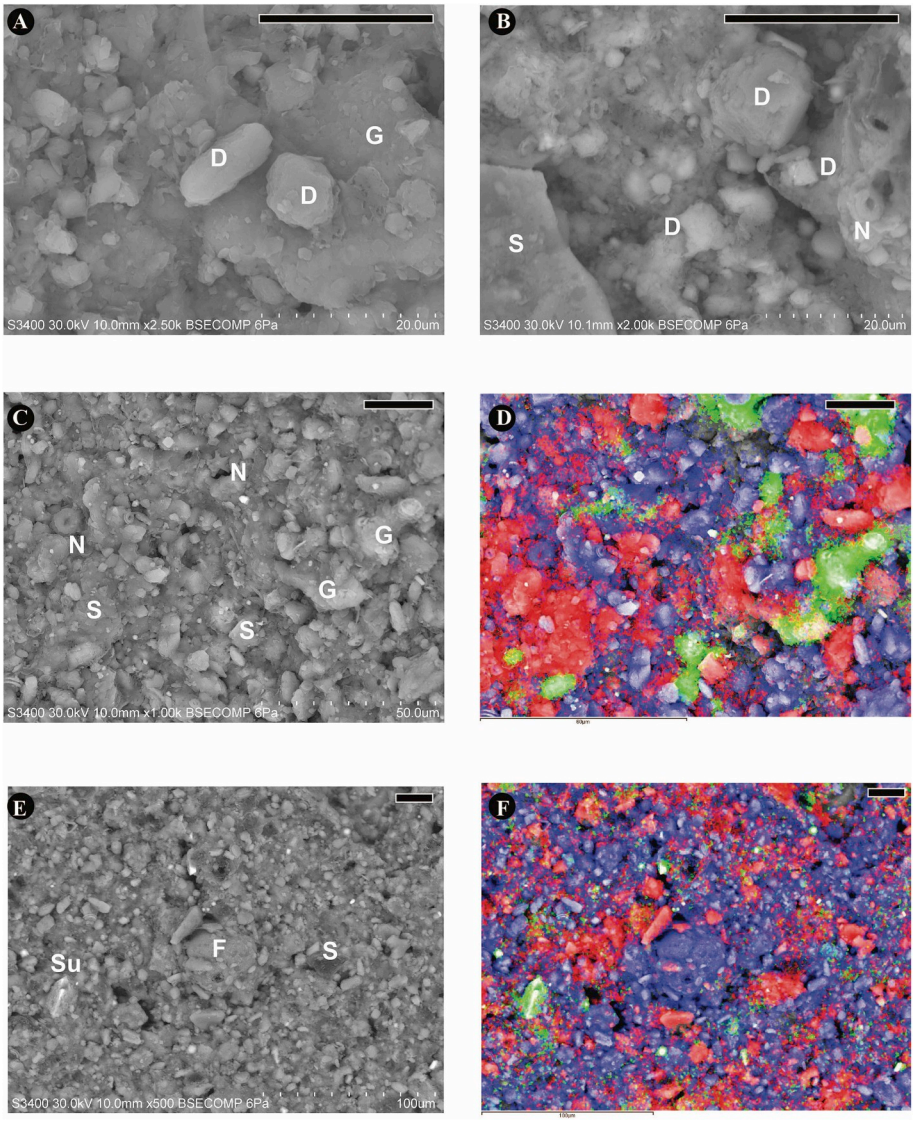

Fig. 6. Digital photographs obtained with scanning electron microscopy combined with energy-dispersive X-ray spectrometry (SEM-EDX). The black bar in the right upper corner corresponds to 20 μm and the magnification is in the bottom right corner of the images. The colors in the EDX images represent the distribution of selected elements on the surface (~upper 100 μm) of the samples: The blue color represents areas dominated by calcium (Ca) and correspond mainly with coccoliths, nannofossils and micron-sized authigenic carbonates; The red color is silicon (Si) and shows area occupied by silicates; The green color is sulfur (S) and corresponds to area covered by sulfates [e.g. gypsum] and sulfides. A) close-up of (D) micron-sized peloidal and rhombohedric dolomite particle on top of (G) a larger tabular gypsum particle (sample from the bottom of the fluid mud; Niskin bottle 21). B) close-up of sediment sample from the gravity core (2.50 m below the seafloor) showing (S) the edge of a large siliciclastic particle, (D) micron-sized dolomite rhombs, and (N) nannofossils. C) and D) SEM-EDX photo of sample from Niskin bottle 8 showing a mixture of micron-sized carbonate particles (the majority) that include (N) nannofossils, and particles of (S) siliciclastic/volcanic components and (G) gypsum. E) and F) SEM-EDX photo of sample from the gravity core (2.50 m below the seafloor) showing (F) a large foraminifer at the center, (Su) an euhedral sulfide crystal in the lower left corner and a majority of micron-sized calcite particles mixed with (S) tens-of-microns-sized siliciclastic and volcanic particles. (For interpretation of the references to color in this figure legend, the reader is referred to the Web version of this article.)

Pleistocene layers exposed all around the steep walls and rims of the horseshoe shaped Urania Basin (Fig. 1B). Therefore, we suggest the alternative explanation that fluids and particles derive from different sources. For instance, the particles could have been originally part of the sedimentary deposits exposed along the steep walls and the rim of the basin. Violent expulsions of fluids possibly associated with large earthquakes, could have caused a collapse of entire sections of the seafloor, which in turn would have caused the re-sedimentation of large volumes of Pliocene and Pleistocene deposits. This hypothesis does not exclude that some of the material (e.g. the large fragment of gypsum-cemented biosiliceous sediment) could have also traveled with the fluids and that new material falling in from the rims of the basin, including the middle late Pleistocene coccoliths that are very abundant in the upper part of the fluid mud, is continuously added to the system (Table 4). The lack of mid Pleistocene coccoliths could reflect a hiatus in the original source sediments and less likely selective dissolution of placoliths of this age. Moreover, the presence of modern coccoliths mixed with fossil taxa suggests that some of the particles could be coming either directly from the photic zone or are re-sedimented from the modern seafloor near the rim of the basin (Table 4).

5.3. The paradox of the Urania Basin's expanded seafloor

As such, the finding of a ~110 m thick, high-density fluid mud that has been in suspension for decades (possibly centuries) in a DHAB is by itself a fascinating discovery but it is not a unique phenomenon in the geologic record. For instance, the remobilization of coccolith sediments by the Storegga Slide, one of the largest scars in Quaternary history (7.2 ^{14}C ka BP), could have produced a giant lake-like area filled with dense turbid bottom water from which the placoliths took years to settle; pore water geochemistry at this location suggests that the sediments are still dewatering after thousands of years (Paull et al., 2010). Similarly, in the hypersaline waters of the Urania Basin, settling of particles is massively attenuated; according to the Stokes Law, in laminar flow conditions, an isolated placolith (6 μm) composed of calcite (2.65 g/cm^3) in higher than seawater salinity (~1.1 g/cm^3) and with molecular viscosity μ of about 10^{-3} kg/m s, will settle extremely slowly (~20 μm/s). However, the samples recovered from the fluid mud and recovered by coring are not only composed of micron-sized calcite placoliths but also by other particles with different compositions and sizes (Table 1). For instance, a 40 μm size particle (one of the 3 main modes detected by the LPSA; Table 1) of gypsum (density 2.31 g/cc) would settle at ~0.05 cm/s which is more than one order of magnitude faster than the settling velocity of a 6 μm placolith. A 40 μm particle composed of feldspar (2.62 g/cc) would settle even faster (~0.08 cm/s). Feldspars and gypsum particles of very fine sand size (125 μm) have settling velocities of ~0.5 cm/s and ~0.8 cm/s which are two orders of magnitude higher than settling velocities for micron-sized calcite placoliths.

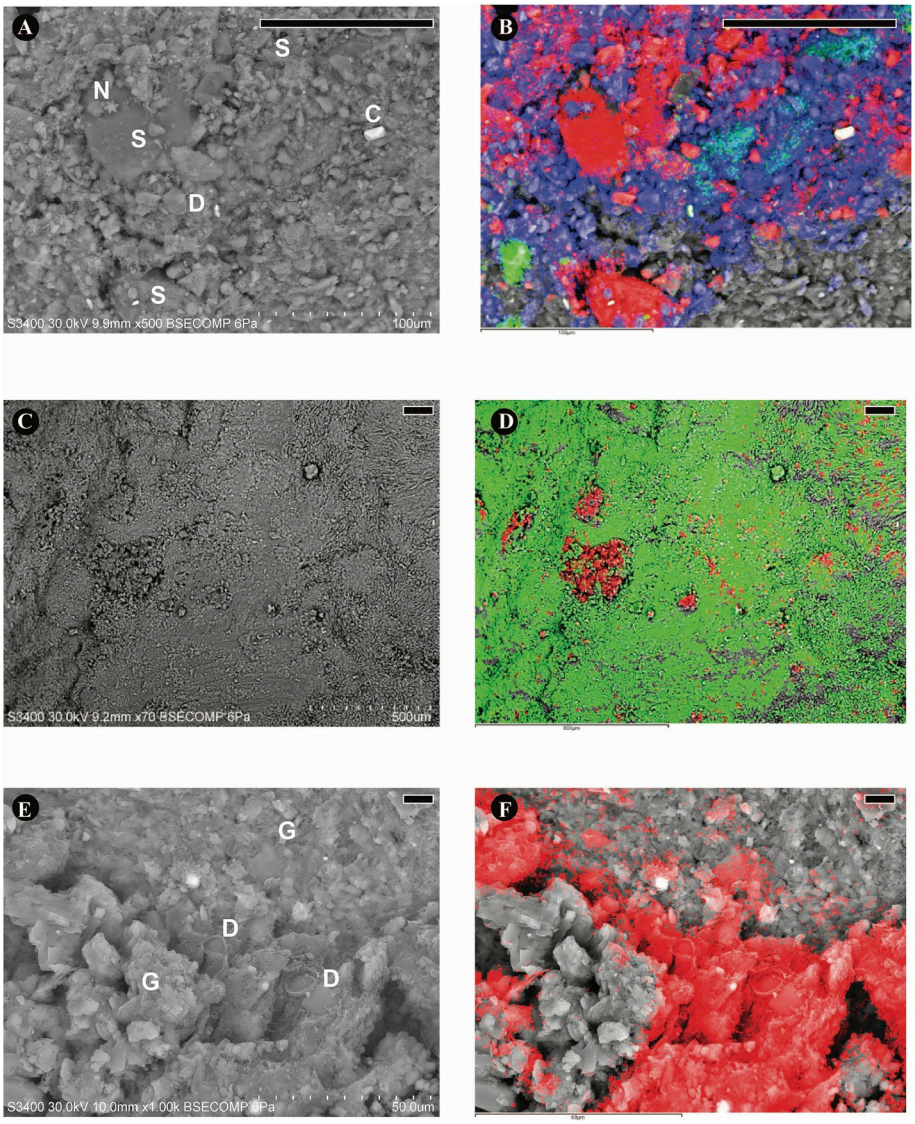

Fig. 7. SEM-EDX digital photographs; the colors represent the same elements as in Fig. 6. The black bar in the right upper corner corresponds to 100 μm and the magnification is in the bottom right corner of the images. A) and B) Sample from the gravity core (2.5 m below the seafloor) showing (S) large siliciclastic particles (in the upper left corner), (N) nannofossils and mixture of micron-sized carbonate and silica-rich particles in the background. Note the bright, prismatic crystal of (C) celestite in the upper right corner. C) and D) overview of a large fragment composed of mainly gypsum and anhydride recovered in the gravity core (4.1 m below the seafloor; Fig. 3B). Intersecting radial growth patterns of gypsum crystals are clearly visible in the upper right corner. E) and F) Close up of the fragment. The area covered in red shows mainly (D) whole and broken centric and pennate diatom valves, which are cemented by the euhedral crystal of (G) gypsum and anhydride (the gray background). Diatoms are rare occurrence in both the samples form the fluid mud and the core and they have been found in large amounts and well-preserved only in this sample suggesting a different source than for the rest of the material recovered. (For interpretation of the references to color in this figure legend, the reader is referred to the Web version of this article.)

Given the mixture of sizes, shapes and densities of the particles in the fluid mud, one would expect to find evidence of particle segregation whereby the coarser and denser particles would be more concentrated in the bottom part of the fluid mud and in the unconsolidated sediments below. However, except for the large gypsum fragment found at the bottom of the pit, there is no evidence of differential settling of particles. These observations support the model results by Goldhammer et al. (2015) which suggest median stream velocities (0.14 m/s) for the fluid mud, velocities that are two orders of magnitude larger than the fastest calculated settling velocity for very-fine-sand size siliciclastic particles. In other words, vigorous mixing due to thermal convection is effective enough that can keep all particle size ranges and types observed in the Urania Basin's fluid mud in suspension hampering any differential settling and segregation based on particle, size, shape or density. Moreover, the lack of accelerating mechanisms (e.g., repackaging of finely dispersed material into compact and dense fecal pellets by zooplankton) precludes the agglomeration of particles further hampering settlement.

6. Conclusions

The floating fluid mud of the Urania Basin provides a model system where gravity-driven sedimentation and sediment compaction are suspended or greatly attenuated. As a result, while the geochemical zonation above the fluid mud is very sharp, the geochemical boundary towards the consolidated bottom sediments is rather gradual. The expulsion of fluidized fine-grained sediment in normal seawater produces conically- or domelike-shaped mud volcanoes and mud flows. When sediments and hot fluids are added to a high-density medium and in a confined seafloor depression like the Urania DHAB, coccolith-sized particles and micro-sized authigenic carbonate particles formed as by-products of microbial activity (e.g. AOM) could mix vertically with the existing brine waters and stay in suspension for long time before falling out, thus producing an apparent vertical expansion of the seafloor floating several tens of meters into the water column.

The sedimentological evidence presented in this study points to separate origins for the bulk of the particles in the fluid mud and the fluids in which they are suspended. Our data lends support to a concept that the source of the biogenic particles are post-Messinian pelagic deposits such as those exposed along the walls and the rim region of the horseshoe-shaped Urania Basin. We hypothesize that catastrophic gravity failures and mass mobilization of the post-Messinian sedimentary layers were likely triggered by earthquake activity, which is very common in the region. Today, Urania Basin seems frozen in time, perhaps for hundreds of years, because of both, the highly dense brine fluids and the continuous mixing by thermal convection. Based on the similarities in particle sizes and compositions, the mixing that occurs in the fluid mud is probably also acting in the firmer sediments that have

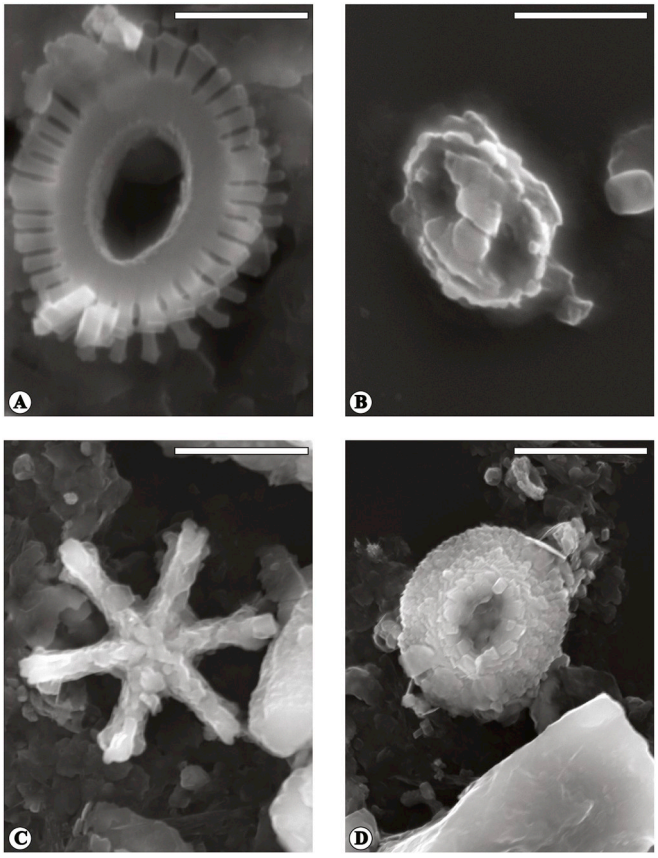

Fig. 8. SEM photographs of common taxa identified in the Urania Basin fluid mud: A) and B) The white bar in the right upper corner corresponds to 1 μm.A) *E. huxleyi*; B) *G. ericsonii*; C) and D) The white bar in the right upper corner corresponds to 5 μm.C) *D. surculus*; D) *Reticulofenestra pseudoumbilicus*.

been recovered by coring below the fluid mud making the bottom of the Urania Basin a very unconventional type of seafloor. Convection could be also vigorous in the Urania Basin's pit where temperatures larger than the 55 °C measured by Corselli et al. (1998) in the top part of the fluid mud can occur.

Similar floating seafloors can occur in other DHABs (e.g. the Chephren 'muddy brine'; Dupré et al., 2010; Dupré et al., 2014), and potentially in other confined seafloor depressions in which fine-grained sediments are resuspended in water columns with higher than seawater densities. Although modern floating seafloors are probably limited to fewer and unique settings associated with the DHABs, they could have been more common and widespread in the geologic past, especially during the formation of shallow-water evaporative basins such as those formed during the Messinian salinity crisis.

Such "low gravity/high density" environments of solid particulates suspended and floating in dense hypersaline fluids provide unusual controls on the stratification and specialization of microbial communities, and potentially the advection of prokaryotes from the subseafloor to the water column. As such the Urania Basin could constitute a model system for 'low gravity/high density' deep ocean environments in extraterrestrial bodies (Marion et al., 2003).

Acknowledgements

We are grateful to the scientists and ship crews of the RV Meteor cruise M84/1 (DARCSEAS). The expedition has been funded through the Deutsche Forschungsgemeinschaft. The laboratory work of this study was funded by the European Research Council under the European Union's Seventh Framework Program – "Ideas" Specific Program, ERC grant agreement # 247153 (Advanced Grant DARCLIFE; PI K.-U.H.). We acknowledge the technical support by Susanne Alfken, Michelle Drake, Julie Kuo, Xavier Prieto Mollar, Silvana Pape, Jessica Schmal and Jenny Wendt during data acquisition and analysis. We are also grateful to Christina Ravelo for comments on an earlier version of the manuscript and to Catherine Pierre for a thorough review of this manuscript.

Appendix A. Supplementary data

Supplementary data to this article can be found online at https://doi.org/10.1016/j.dsr2.2019.07.014.

References

Hsü, K.J., Montadert, L., Bernoulli, D., Bizon, G., Cita, M.B., Erickson, A., Fabricius, F., Garrison, R.E., Kidd, R.B., Mélières, F., Müller, C., Wright, R.C., 1978. Site 374: Messina abyssal plain. In: Kidd, R.B., Worstell, P.J. (Eds.), Init. Rep. DSDP XLII (Part 1), pp. 175–217. https://doi.org/10.2973/dsdp.proc.42-1.105.1978.

Aiello, I.W., Ravelo, A.C., 2012. Evolution of marine sedimentation in the bering sea since the Pliocene. Geosphere 8 (6), 1231–1253.

Aloisi, G., Cita, M.B., Castradori, D., 2006. Sediment Injection in the Pit of the Urania Anoxic Brine Lake (Eastern Mediterranean): Rend, vol. 17. Acc. Naz. Lincei, CL. Sci. Fis., Roma, pp. 243–262.

Antunes, A., Ngugi, D.K., Stingl, U., 2011. Microbiology of the Red Sea (and other) deep-sea anoxic brine lakes. Environ Microbiol. Rep. 3 (4), 416–433.

Baker, P.A., Bloomer, S.H., 1988. The origin of celestite in deep-sea carbonate sediments. Geochem. Cosmochim. Acta 52, 335–339.

Beckman Coulter Inc., 2003. LS 13 230 Particle Size Analyzer Manual PN 7222061A. Particle Characterization Group, Miami, Florida.

Borin, S., Brusetti, L., F., Mapelli, G., D'Auria, T., Brusa, M., Marzorati, A., Rizzia, M., Yakimov, D., Marty, G.J., De Lange, P., Van der Wielen, H., Bolhuis, T.J., McGenity, P.N., Polymenakou, E., Malinverno, L., Giuliano, C., Corselli, Daffonchio, D., 2009. Sulfur cycling and methanogenesis primarily drive microbial colonization of the highly sulfidic Urania deep hypersaline basin. Proc. Natl. Acad. Sci. U. S. A 106, 9151–9156. https://doi.org/10.1073/pnas.0811984106.

Burd, A.B., Jackson, G.A., 2009. Particle aggregation. Annual Reviews of Marine Science 1, 65–90.

Charlou, J.L., Donval, J.P., Zitter, T., Roy, N., Jean-Baptiste, P., Foucher, J.P., Woodside, J., MEDINAUT Scientific Party, 2003. Evidence of methane venting and geochemistry of brines on mud volcanoes of the Eastern Mediterranean Sea. Deep-Sea Res. 50, 941–958.

Cita, M.B., 2006. Exhumation of Messinian evaporites in the deep-sea and creation of deep anoxic brine-filled collapsed basins. Sediment. Geol. 188/89, 327–378. https://doi.org/10.1016/j.sedgeo.2006.03.013.

Corselli, C., Aghib, F.S., 1987. Brine formation and gypsum precipitation in the bannock basin, eastern mediterranean. Mar. Geol. 75 (1–4), 185–199.

Corselli, C., Basso, D., De Lange, G.J., Thomson, J., 1996. Mediterranean ridge accretionary complex yields rich surprises. EOS 77, 227.

Corselli, C., Della Vedova, B., Camerlenghi, A., De Lange, G.J., Westbrook, G.K., 1998. Emission of warm fluids and high temperature in the Urania basin: observations from 1993 to 1998. In: International Workshop 'Extreme Marine Environments' GEOMAR Kiel, 19–22 November 1998, Volume of Abstracts, pp. 9–10.

Daffonchio, D., Borin, S., Biodeep Scientific Party, 2006. Stratified prokaryote network in the oxic–anoxic transition of a deep sea halocline. Nature 440, 203–207.

Dezileau, L., Bareille, G., Reyss, J.L., Lemoine, F., 2000. Evidence for strong sediment redistribution by bottom currents along the southeast Indian ridge. Deep Sea Res. Oceanogr. Res. Pap. 47 (10), 1899–1936.

Dubois, N., Mitchell, N.C., 2012. Large-scale sediment redistribution on the equatorial Pacific seafloor. Deep Sea Res. Oceanogr. Res. Pap. 69, 51–61.

Dupré, S., Woodside, J., Klaucke, I., Mascle, J., Foucher, J.P., 2010. Widespread active seepage activity on the Nile Deep Sea Fan (offshore Egypt) revealed by high-definition geophysical imagery. Mar. Geol. 275, 1–19. https://doi.org/10.1016/j.margeo.2010.04.003.

Dupré, S., Mascle, J., Foucher, J.P., Harmegnies, F., Woodside, J., Pierre, C., 2014. Warm brine lakes in craters of active mud volcanoes, Menes caldera off NW Egypt: evidence for deep-rooted thermogenic processes. Geo Mar. Lett. 34 (2–3), 153–168.

Dutkiewicz, A., Müller, R.D., Hogg, A.M., Spence, P., 2016. Vigorous deep-sea currents cause global anomaly in sediment accumulation in the Southern Ocean. Geology 44 (8), 663–666.

Eder, W., Ludwig, W., Huber, R., 1999. Novel 16S rRNA gene sequences retrieved from highly saline brine sediments of Kebrit Deep. Red Sea: Arch. Microbiol. 172, 213–218.

Edgcomb, V., Orsi, W., Leslin, C., Epstein, S.S., Bunge, J., Jeon, S., Yakimov, M.M., Behnke, A., Stoeck, T., 2009. Protistan community patterns within the brine and halocline of deep hypersaline anoxic basins in the eastern Mediterranean Sea. Extremophiles 13, 151–167.

Eppley, R.W., Peterson, B.J., 1979. Particulate organic matter flux and planktonic new production in the deep ocean. Nature 282, 677–680.

Fildani, A., Clark, J., Covault, J.A., Power, B., Romans, B.W., Aiello, I.W., 2018. Muddy sand and sandy mud on the distal Mississippi fan: implications for lobe depositional

processes. Geosphere 14 (3), 1051–1066.
Fusi, N., Aloisi de Larderel, G., Borello, A., Amelio, O., Castradori, D., Negri, A., Rimoldi, B., Sanvoisin, R., Tarbini, P., Cita, M.B., 1996. Marine geology of the MEDRIFF corridor, Mediterranean Ridge: isl. Arc 5, 420–439.
Goldhammer, T., Schwärzle, A., Aiello, I.W., Zabel, M., 2015. Temporal stability and origin of chemoclines in the deep hypersaline anoxic Urania basin. Geophys. Res. Lett. 42 (12), 4888–4895.
Hesse, R., Schacht, U., 2011. Early diagenesis of deep-sea sediments. In: Developments in Sedimentology, vol. 63. Elsevier, pp. 557–713.
Hübner, A., De Lange, G.J., Dittmer, J., Halbach, P., 2003. Geochemistry of an exotic sediment layer above sapropel S-1: mud expulsion from the Urania Basin, Eastern Mediterranean? Mar. Geol. 197, 49–61.
Inthorn, M., Wagner, T., Scheeder, G., Zabel, M., 2006. Lateral transport controls distribution, quality and burial of organic matter along continental slopes in high-productivity areas. Geology 34 (3), 205–208. https://doi.org/10.1130/G22153.1.
Jongsma, D., Fortuin, A.R., Huson, W., Troelstra, S.R., Klaver, G.T., Peters, J.M., Van Harten, D., De Lange, G.J., Ten Haven, L., 1983. Discovery of an anoxic basin within the strabo trench, eastern mediterranean. Nature 305 (5937), 795.
Karisiddaiah, S.M., 2000. Diverse methane concentrations in anoxic brines and underlying sediments, eastern Mediterranean Sea. Deep Sea Res. I 47, 1999–2008.
Konert, M., Vandenberghe, J., 1997. Comparison of laser grain size analysis with pipette and sieve analysis: a solution for the underestimation of the clay fraction. Sedimentology 44, 523–535. https://doi.org/10.1046/j.1365-3091.1997.d01-38.x.
Kopf, A., Robertson, A.H.F., Clennell, M.B., Flecker, R., 1998. Mechanism of mud extrusion on the Mediterranean Ridge accretionary complex. Geo Mar. Lett. 18, 97–114.
Le Pichon, X., Henry, P., the Kaiko-Nankai Scientific Crew, 1991. Water budgets in accretionary wedges: a comparison. Philos. Trans. R. Soc. Lond. 335, 315–330.
Loncke, L., Gaullier, V., Mascle, J., Vendeville, B., Camera, L., 2006. The Nile deep-sea fan: an example of interacting sedimentation, salt tectonics, and inherited subsalt paleotopographic features. Mar. Pet. Geol. 23, 297–315.
Marion, G.M., Fritsen, C.H., Eicken, H., Payne, M.C., 2003. The search for life on Europa: limiting environmental factors, potential habitats, and earth analogues. Astrobiology 3, 785–811.
McCave, I.N., 2008. Nepheloid layers. In: Encyclopedia of Ocean Sciences (Revised Online Edition). Academic Press, London, pp. 8–18.
McCave, I.N., Hall, I.R., Bianchi, G.G., 2006. Laser vs. settling velocity differences in silt grain- size measurements: estimation of palaeocurrent vigor. Sedimentology 53, 919–928. https://doi.org/10.1111/j.1365-3091.2006.00783.x.
MEDRIFF Consortium, 1995. New discovery of brine lakes in the seafloor of the Eastern Mediterranean. EOS 76, 313.
Milkov, A.V., 2000. Worldwide distribution of submarine mud volcanoes and associated gas hydrates. Mar. Geol. 167, 29–42.
Paull, C.K., Ussler, W., Holbrook, W.S., Hill, T.M., Haflidason, H., Winters, W., Lorenson, T., Aiello, I.W., Johnson, J., Ludsten, E., 2010. The Tail of the Storegga Slide: insights from the geochemistry and sedimentology of the Norwegian Basin deposits. Sedimentology. https://doi.org/10.1111/j.1365-3091.2010.01150.x.
Pierre, C., Bayon, G., Blanc-Valleron, M.M., Mascle, J., Dupré, S., 2014. Authigenic carbonates related to active seepage of methane-rich hot brines at the Cheops mud volcano, Menes caldera (Nile deep-sea fan, eastern Mediterranean Sea). Geo Mar. Lett. 34 (2–3), 253–267.
Poppe, L.J., Paskevich, V.F., Hathaway, J.C., Blackwood, D.S., 2001. A laboratory manual for X-ray powder diffraction. US Geological Survey Open-File Report 1 (041), 1–88.
Pujos, A., Giraudeau, J., 1993. Répartition des Noelaerhabdaceae (nannofossiles calcaires) dans le Quaternaire moyen et supérieur des océans Atlantique et Pacifique. Oceanol. Acta 16, 349–362.
Rothwell, R.G., 1989. Minerals and Mineraloids in Marine Sediments: an Optical Identification Guide. Elsevier, London, pp. 279.
Shokes, R.F., Trabant, P.K., Presley, B.J., Reid, D.F., 1977. Anoxic, hypersaline basin in the northern Gulf of Mexico. Science 196 (4297), 1443–1446.
Toledo, F.A., Quadros, J.P., Camillo Jr., E., Santarosa, A.C.A., Flores, J.A., Costa, K.B., 2016. Plankton biochronology for the last 772,000 years from the western south atlantic ocean. Mar. Micropaleontol. 127, 50–62.
Triantaphyllou, M.V., Ziveri, P., Gogou, A., Marino, G., Lykousis, V., Bouloubassi, I., Emeis, K.C., Kouli, K., Dimiza, M., Rosell-Mele, A., Papanikolaou, M., 2009. Late glacial–holocene climate variability at the south-eastern margin of the aegean sea. Mar. Geol. 266 (1–4), 182–197.
Van der Wielen, P.W.J.J., Bolhuis, H., Borin, S., Daffonchio, D., Corselli, C., Giuliano, L., D'Auria, G., De Lange, G.J., Huebner, A., Varnavas, S.P., Thomson, J., Tamburini, C., Marty, D., McGenity, T.J., Timmis, K.N., Party, B.S., 2005. The Enigma of Prokaryotic Life in Deep Hypersaline Anoxic Basins. Science, vol. 307, 121–123.
Vengosh, A., Starinsky, A., 1993. Relics of evaporated sea water in deep basins of the eastern Mediterranean. Mar. Geol. 115 (1–2), 15–19.
Vengosh, A., De Lange, G.J., Starinsky, A., 1998. Boron isotope and geochemical evidence for the origin of Urania and Bannock brines at the eastern Mediterranean: effect of water-rock interactions. Geochem. Cosmochim. Acta 62, 3221–3228.
Wallmann, K., Suess, E., Westbrook, G.H., Winkler, G., Cita, M.B., MEDRIFF Consortium, 1997. Salty brines on the Mediterranean sea floor. Nature 387, 31–32.
Westbrook, G.K., Reston, T.J., 2002. The accretionary complex of the Mediterranean Ridge: tectonics, fluid flow and the formation of brine lakes. Mar. Geol. 186, 1–8.
Winckler, G., Suess, E., Wallmann, K., de Lange, G.J., Westbrook, G.K., Bayer, R., 1997. Excess helium and argon of radiogenic origin in Mediterranean brine basins. Earth Planet. Sci. Lett. 151 (3–4), 225–231.
Yakimov, M.M., Giuliano, L., Cappello, S., Denaro, R., Golyshin, P.N., 2007. Microbial community of a hydrothermal mud vent underneath the deep-sea anoxic brine lake Urania (Eastern Mediterranean). Orig. Life Evol. Biosph. 37 (2), 177–188.
Zabel, M., Shipboard Scientific Party, 2012. RV METEOR, Cruise Report M84/L1. Biogeochemistry and Methane Hydrates of the Black Sea, Oceanography of the Mediterranean, Shelf Sedimentation and Cold Water Carbonates. DFG Senatskommission für Ozeanographie, pp. 39. https://doi.org/10.2312/cr_m84_1.